

Journal of Materials Chemistry A

Accepted Manuscript



This is an *Accepted Manuscript*, which has been through the Royal Society of Chemistry peer review process and has been accepted for publication.

Accepted Manuscripts are published online shortly after acceptance, before technical editing, formatting and proof reading. Using this free service, authors can make their results available to the community, in citable form, before we publish the edited article. We will replace this *Accepted Manuscript* with the edited and formatted *Advance Article* as soon as it is available.

You can find more information about *Accepted Manuscripts* in the [Information for Authors](#).

Please note that technical editing may introduce minor changes to the text and/or graphics, which may alter content. The journal's standard [Terms & Conditions](#) and the [Ethical guidelines](#) still apply. In no event shall the Royal Society of Chemistry be held responsible for any errors or omissions in this *Accepted Manuscript* or any consequences arising from the use of any information it contains.

3D Hierarchical Porous Zinc-Nickel-Cobalt Oxides Nanosheets Grown on Ni Foam as Binder-Free Electrodes for Electrochemical Energy Storage

Huixin Chen ^{a, 1}, Qiaobao Zhang ^{b, d, 1}, Xiang Han ^c, Junjie Cai ^b, Meilin Liu ^d, Yong Yang ^{a, *},
Kaili Zhang ^{b, *}

^a State Key Laboratory for Physical Chemistry of Solid Surfaces, Department of Chemistry, Xiamen University, Xiamen, 361005, P. R. China

^b Department of Mechanical and Biomedical Engineering, City University of Hong Kong, 83 Tat Chee Avenue, Kowloon, Hong Kong

^c Semiconductor Photonics Research Center, Department of Physics, Xiamen University, Xiamen, 361005, P. R. China

^d School of Materials Science and Engineering, Georgia Institute of Technology, 771 Ferst Drive, Atlanta 30332-0245, GA, United States

¹ These authors contributed equally to this work

*Corresponding authors:

Yong Yang, E-mail address: yyang@xmu.edu.cn

Kaili Zhang, E-mail address: kaizhang@cityu.edu.hk

Abstract

Three-dimensional (3D) hierarchically porous transition metal oxides, particularly those involving different metal ions of mixed valence states and constructed from interconnected nano-building blocks directly grown on conductive current collectors, are promising electrode candidates for energy storage devices such as Li-ion batteries (LIBs) and supercapacitors (SCs). This study reports a facile and scalable chemical bath deposition process combined with simple calcination for fabricating 3D hierarchically porous Zn–Ni–Co oxide (ZNCO) nanosheet arrays directly grown on Ni foam with robust adhesion. The resulting nanostructures are then evaluated as a binder-free electrode for LIBs and SCs. Given its unique architecture and compositional advantages, the electrode exhibits a reversible capacity of 1131 mAh g⁻¹ after 50 cycles at a current density of 0.2 Ag⁻¹, an excellent long-term cycling stability at a high current density of 1 Ag⁻¹ for 1000 cycles, and a desirable rate capability when tested as an anode for LIBs. When used for SCs, the electrode demonstrates a high specific capacitance (1728 Fg⁻¹ at 1 Ag⁻¹), an outstanding rate capability (72% capacitance retention from 1 Ag⁻¹ to 50 Ag⁻¹), and an excellent cycling stability (capacitance of 1655 Fg⁻¹ after 5000 cycles at a current density of 20 Ag⁻¹ with 108.6% retention). Overall, the unique 3D hierarchically porous ZNCO nanosheets hold a great promise for constructing high-performance energy storage devices.

Keywords: Zinc–nickel–cobalt oxides nanosheets; Porous structure; Lithium ion batteries; Supercapacitors

1. Introduction

With the deterioration of the environment and ever-growing energy demand, an ever increasing and urgent demand has emerged for the development of efficient electrochemical energy storage devices with high energy density, power density, and safety.¹⁻⁸ Given their superior electrochemical performance, safety characteristics, and ecological features, Li-ion batteries (LIBs) and supercapacitors (SCs) have attracted considerable attention as major devices for electrochemical energy storage because of their great promise as power sources for diverse applications, ranging from portable electronics to electric vehicles (EVs) or hybrid EVs.⁸⁻¹⁵ It is now well documented that the performance of these devices depends heavily on the properties of their materials and the key for achieving outstanding performance of these devices is to seek appropriate materials and suitably design the electrode structure.^{11,14,16-18} Nanostructured transition metal oxides (TMOs) have been intensively investigated as promising electrode materials for LIBs and SCs because of their high specific capacities/capacitances, suitability for large-scale fabrication, and rich redox reactions involving different ions.^{2,10,15,16,18-28} In particular, mixed TMOs (MTMOs) from the combination of multiple transition metal cations with stoichiometric or even non-stoichiometric compositions in the form of nanostructures are emerging as high-performance electrode materials for electrochemical energy storage because of their several advantages over simple TMOs; in particular, MTMOs exhibit higher electrochemical activities and stronger electronic conductivity than TMOs, making the former more favorable for applications in high-performance electrochemical energy storage than the latter.^{16,23,25,29-31} However, the commercialization of MTMOs is limited by their intrinsic electron conductivity and structural stability that are insufficient to sustain large volume changes during repeated discharge-charge processes.¹⁶

Scrupulous design and construction of well-defined hierarchically porous structures of MTMOs composed of nanosized building blocks that are directly grown on conductive current collectors are needed to circumvent these issues and optimize the electrochemical performance of these materials in LIBs and SCs.^{16,29,32} The hierarchically porous structures of MTMOs provide an efficient pathway for electron transport, shorten the ion diffusion path, enable the full exposure and rich accessibility of electroactive sites to the electrolyte, and buffer the volume change during repeated charge–discharge processes.^{29,33} Directly growing these structures on conductive current collectors can overcome their intrinsic poor conductivity and eliminate the need for electrode additives and the added step of slurry casting during electrode fabrication, which extremely favor the development of high-performance electrode materials.^{17,23,29,34} Researchers have demonstrated that hierarchically porous structures of self-supported MTMOs constructed from nanosized building blocks can realize the full performance potential of materials when the aforementioned design rationales are integrated.^{16,29,35–38} Hence, these materials hold a great promise as high-performance electrodes for electrochemical energy storage. Notwithstanding these advances, great challenges remain for the fabrication of hierarchically porous MTMO structures with complex chemical compositions that are directly grown on the current collector through simple and easy scale-up approaches to achieve enhanced electrochemical performance. Currently, the most commonly used solution-based methods to synthesize self-supported MTMOs are hydrothermal methods, in which the reactions are conducted in a solution on a pressurized sealed container (autoclave) at a relatively high reaction temperature (normally higher than 100 °C) and a long duration (longer than 4 h); these conditions make MTMO synthesis unlikely to be scaled up in low cost and hinder the practical applications of

nanostructured MTMOs.³⁹ Therefore, methods that are simple to perform, easy to scale up, cost efficient, and allow growth at a relatively low temperature are still highly desirable.

Partially substituting Co in Co_3O_4 by low-cost and eco-friendly alternative elements such as Zn and Ni to form mixed Co oxides can significantly enhance electrochemical performance when applied as electrodes for electrochemical energy storage; this partial substitution offers an effective way to construct high-performance electrodes for both LIBs and SCs.¹⁶ Enlightened by the promising findings of previous studies, we present for the first time a facile and scalable chemical bath deposition (CBD) strategy combined with a simple calcination treatment to fabricate 3D hierarchically porous architectures of Zn–Ni–Co oxide (ZNCO) nanosheets composed of numerous highly crystalline nanoparticles directly grown on Ni foam as binder-free high-performance electrode materials for LIBs and SCs. The synthesized method is simple, low-cost, easy to scale-up, and allows growth at a low temperature without using high pressure and special apparatus. The as-fabricated hierarchically porous ZNCO nanosheets consist of numerous highly crystalline nanoparticles, leaving a large number of mesopores for fast ion transport and facilitating electrolyte transport. The direct growth of interconnected 2D nanosheets on Ni foam ensures that every nanosheet participates in electrochemical reactions, good mechanical adhesion and, more importantly, good electrical contact with the conductive substrate. As a result, the resultant integrated electrodes, with their advantageous structural features and compositional advantages, exhibit better electrochemical performances in terms of specific capacity and rate capability when applied as electrodes for LIBs compared with binary ZnCo_2O_4 (ZCO), NiCo_2O_4 (NCO), and ZNCO nanosheet-pasted electrodes. Moreover, these electrodes are superior to ZCO, NCO and Co_3O_4 (CO) electrodes in terms of specific capacitance and cycling stability even at a high charge/discharge current density when applied in SCs.

2. Experimental Section

2.1 ZNCO nanosheet preparation on Ni foam

In a typical procedure, the as-cleaned substrate (3D porous Ni foam) with backsides coated with polyimide tape was immersed into a closed 600 mL Pyrex beaker with a 400 mL aqueous solution containing 27.655 g of urea, 0.878 g (0.01 M) of Zn acetate dehydrate, 3.981 g (0.04 M) of Ni(II) acetate tetrahydrate, and 9.963 g (0.1 M) of Co(II) acetate tetrahydrate. The beaker containing the growth solution and substrates was covered with an aluminum foil, placed in an oven, and then maintained at 90 °C for 2 h. After the beaker naturally cooled down to room temperature, the substrates were removed from the solution, rinsed with distilled water, and then ultrasonically cleansed with distilled water for several times. Finally, the as-fabricated samples were annealed at 350 °C in normal argon gas for 2 h to obtain hierarchically porous architectures of ternary ZNCO nanosheets.

2.2 Sample characterization

The morphology, crystalline structure, and composition of the as-grown ZNCO nanosheets were characterized using field-emission scanning electron microscopy (Hitachi S4800), transmission electron microscopy (FEI Tecnai G2 20 TEM), and X-ray diffraction (Rigaku SmartLab, XRD). The thermal behavior and porous characteristics of the samples were tested using a thermogravimetric analysis instrument (SDT Q600 Thermo Gravimetric/Differential Thermal Analyzer) and a Brunauer–Emmett–Teller (BET) surface area analyzer (Micromeritics TriStar II 3020). Elements analysis for metals was performed using an Agilent 4500 quadrupole inductively coupled plasma mass spectrometer (ICP-MS).

2.3 Electrochemical performance evaluation

The as-synthesized hierarchical ZNCO nanosheet arrays directly grown on the Ni foam substrate

as a working electrode (ZnCO nanosheets/Ni foam electrode) were dried in vacuum for 12 h at 120 °C to test their electrochemical performance as anodes for LIBs. The cells (CR2025) were assembled in a glovebox (MBRAUN, LABmaster 100, Germany) under an argon atmosphere. The counter and reference electrodes were Li metal foil (15 mm in diameter), and the electrolyte solution was 1 M LiPF₆ (EC:DMC:EMC = 1:1:1, in volume). The cells were charged and discharged over a voltage range of 0.01–3 V (versus Li⁺/Li) at room temperature by using the Land CT2001A system (Wuhan, China). Cyclic voltammetry (CV) was performed on a four-channel multifunctional electrochemical work station (VersaSTAT MC, America), and scanning was conducted from 3.0 V to 0.01 V versus Li/Li⁺ at a rate of 0.1 mV s⁻¹. The mass loading on the electrodes was determined as follows: the mass difference of the Ni foam substrate before and after ZnCO nanosheet deposition was used to determine the mass of ZnCO nanosheets. The Ni foam was first cut into circular disks with a diameter of 14 mm, and the mass of the as-obtained Ni foam circular disk (m_1) and ZnCO nanosheets grown on Ni foam circular disk (m_2) was carefully determined using a microbalancer (Mettler Toledo XS3DU) with an accuracy of 1 μg. The active mass of ZnCO nanosheets was calculated as $m_2 - m_1$. The active mass loading of ZnCO nanosheets on Ni foam was determined to be approximately 2 mg. For comparison, the ZnCO nanosheet-pasted electrode was prepared by mixing ZnCO nanosheet powder (80 wt.%), acetylene black (10 wt.%), and polyvinylidene fluoride as a binder (10 wt.%) in N-methyl pyrrolidone. The slurry of the active material (2 mg) was spread onto a Cu foil (1.5 cm²). Afterward, the sheet was dried under a vacuum at 120 °C for 4 h.

The as-synthesized ZnCO nanosheets on Ni foam were dried overnight at 120 °C under a vacuum and directly used as working electrodes for the SC test. Pt and Hg/HgO electrodes were used as counter and reference electrodes, respectively. The electrochemical tests were conducted

using a CHI 660D electrochemical workstation in a 6 M KOH aqueous solution. The long-term cycling performance was evaluated using an Arbin testing system (MSTAT). The specific capacitance (C) was calculated according to the following equations:

$$C = \frac{I \Delta t}{m \Delta V}$$

where C (F g⁻¹) is specific capacitance, I (mA) represents discharge current, and m (mg), ΔV (V), and Δt (s) designate the mass of the active materials, the potential drop during discharge, and the discharge time, respectively. The mass loading of ZNCO nanosheets on Ni foam for SCs tests is about 1.3 mg cm⁻².

3. Results and Discussion

3.1. Synthesis and characterization of the ZNCO nanosheets on Ni foam

The formation of the hierarchically porous structures of the ZNCO nanosheets supported on Ni foam through CBD combined with a post-annealing treatment is schematically illustrated in Figure 1(a–c). First, high-density hierarchically structured ZNCO-precursor nanosheets were directly grown on Ni foam through a facile and scalable CBD method (Figure 1(b)). The XRD patterns of the as-synthesized ZNCO-precursor nanosheets confirm that they are Co-based carbonate hydroxides (Figure S1, supporting information). These hierarchically structured ZNCO-precursor nanosheets are then converted to hierarchically porous structures of ZNCO through simple thermal annealing (Figure 1(c)). The typical morphology of the ZNCO-precursor nanosheets directly grown on Ni foam is depicted in Figure 1(d–f). As shown in Figure 1(d), the nanosheets are uniformly grown on the skeleton of the Ni foam to form a conformal coating on

the surface over the large area. A close SEM examination (Figure 1(e–f)) demonstrates that these nanosheets with a rippled silk-like shape are interconnected to one another, forming a free-standing network. After thermal annealing, the as-obtained ZNCOs almost inherit the rippled silk-like network structure and morphology of interconnected nanosheets of its corresponding ZNCO precursor (Figure 1(g–i)).

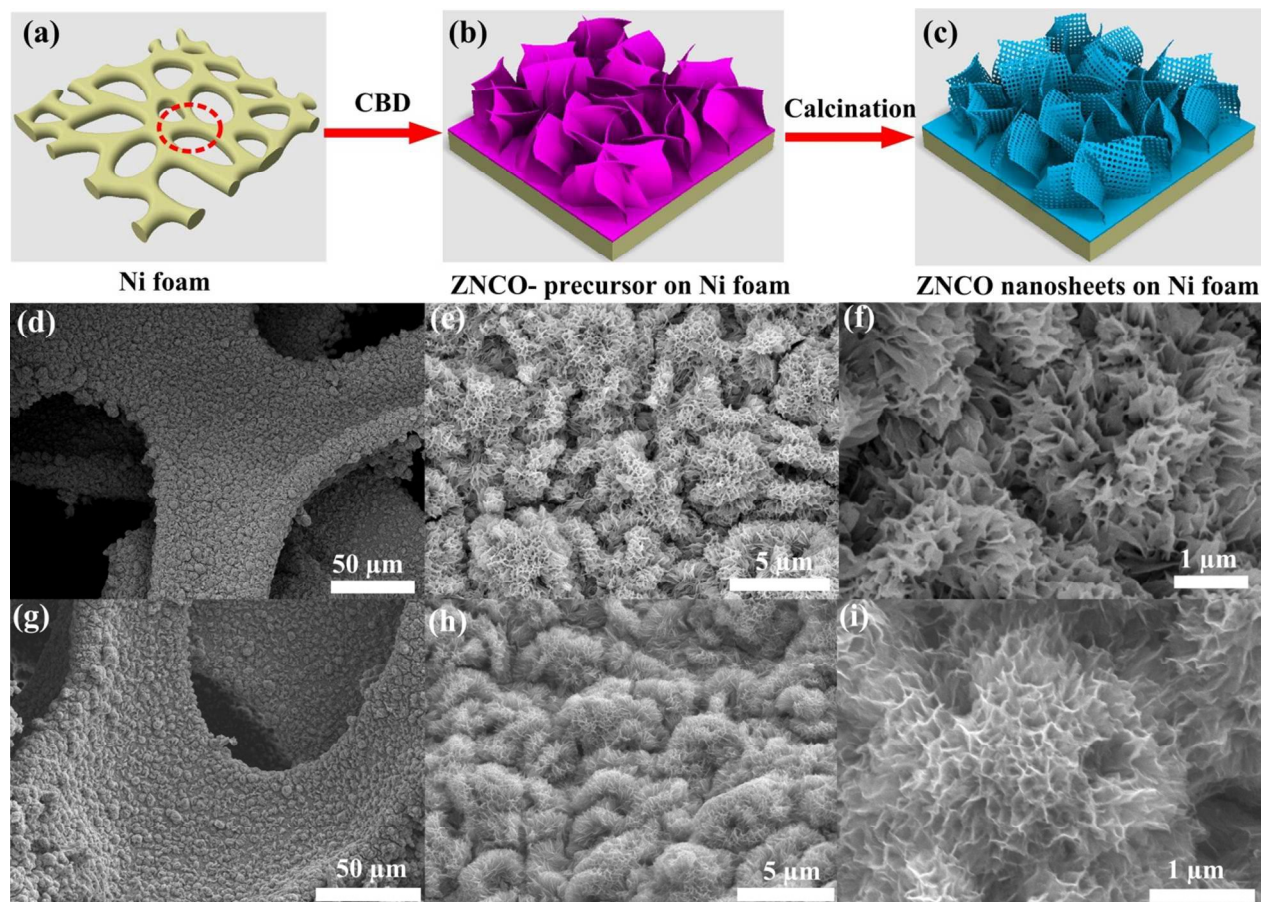


Figure 1. (a–c) Schematic illustration of the formation process of ZNCO nanosheets on Ni foam and SEM images of (d–f) ZNCO-precursor nanosheets and (g–i) ZNCO nanosheets on Ni foam.

The thermal behavior of ZNCO-precursor nanosheets was investigated through DTA-TG, and the result is shown Figure 2(a). Two weight-loss regions below 200 °C and in the range of 200–272 °C can be observed, which may be attributed to the dehydration of physically adsorbed water

and the decomposition of the ZNCO-precursor nanosheets to the ZNCO nanosheets. Thus, the temperature of 350 °C was selected for complete thermal decomposition of the ZNCO-precursor nanosheets to the ZNCO nanosheets. The crystallographic structure and phase purity of the as-synthesized ZNCO nanosheets supported on Ni foam were investigated using XRD. As shown in Figure 2b, aside from the three strong peaks from the Ni foam substrate, all of the reflection peaks can be indexed as a spinel structure phase of the space group $Fd\bar{3}m$, which is isostructural to the well-crystallized spinel Co_3O_4 (PDF #43-1003).^{40,41} This finding demonstrates that the partial replacement of Co ions with Ni and Zn ions does not affect the crystalline structure of spinel Co_3O_4 . The elemental composition of the ZNCO nanosheets directly grown on the Si substrate was examined using energy dispersive X-ray measurements. As shown in Figure 2(c), the nanosheets only produce signal peaks of Zn, Ni, Co, O, and Si with an atomic Zn/Ni/Co ratio of almost 1:1:2, in agreement with the ICP-MS results (Table S1, supporting information). This result indicates the formation of pure $\text{Zn}_{0.75}\text{Ni}_{0.75}\text{Co}_{1.5}\text{O}_4$, whereas the signal of Si originates from the Si substrate. The mesoporous features of the ZNCO nanosheets were examined using N₂ isothermal adsorption–desorption measurements, as depicted in Figure 2d. The figure reveals a typical IV isotherm with a distinct hysteresis loop in the range of 0.7–1.0 P/P₀, indicating its mesoporous structures.⁴⁰ This finding is similar to the TEM observation (Figure 3). The pore size distribution derived from the desorption data and calculated from the isotherm using the BJH model (Figure 2(d)) demonstrates that the ZNCO nanosheets possess a narrow pore size range of 4–12 nm and an average pore diameter of 5.7 nm. This result further confirms the mesoporous feature of the ZNCO nanosheets. The BET specific surface area of the ZNCO nanosheets was measured to be 63.5 m²g⁻¹. Such a feature may favor Li⁺ ion diffusion and electrode–electrolyte contacts during the electrochemical reaction, which enhances their electrochemical performance

as anodes for LIBs.^{40,42}

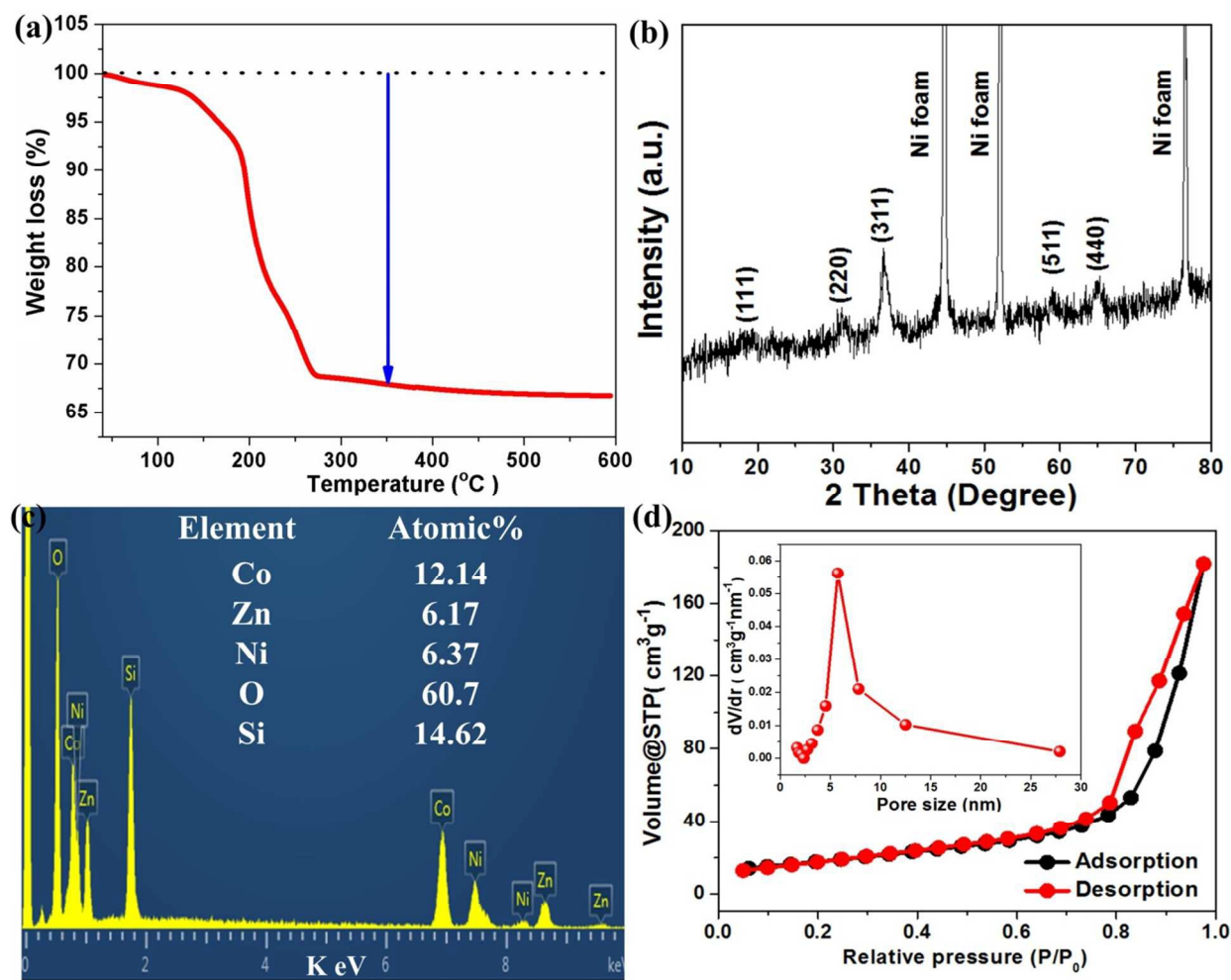


Figure 2. (a) TG-DTA curves of weight loss of ZNCO-precursor nanosheets, (b) XRD patterns of ZNCO nanosheets on Ni foam, (c) EDX spectrum of ZNCO nanosheets on Si substrate and (d) the N₂ adsorption-desorption isotherm of the as-prepared ZNCO nanosheets, the inset is the pore distribution.

The elemental composition and oxidation state of the as-prepared nanosheets were analyzed in detail using X-ray photoelectron spectroscopy, and the corresponding results are presented in Figures 3 and S2. The survey spectrum shown in Figure S2 indicates the presence of Ni, Co, Zn,

O, and C from the reference and the absence of other impurities. As illustrated in Figure 3(a), the high-resolution Co 2p spectrum shows two distinguished doublets located at a low-energy (Co 2p_{3/2}) and high-energy band (Co 2p_{1/2}) along with two couples of shakeup satellites (indicated as “Sat.”). The spin-orbit splitting value of Co 2p_{1/2} and Co 2p_{3/2} is over 15 eV, suggesting the coexistence of Co²⁺ and Co³⁺.⁴³ The high-resolution Ni 2p spectrum is best fitted with two spin-orbit doublets, characteristic of Ni²⁺ and Ni³⁺, and two shakeup satellites.⁴³ For the high-resolution Zn 2p spectrum, two major peaks at 1020.7 and 1043.8 eV are ascribed to the Zn 2p_{3/2} and Zn 2p_{1/2} of Zn(II), respectively. The O 1s peaks at 529.4 and 531.3 eV correspond to the oxygen species in the ZNCO nanosheets. These results show that the ZNCO nanosheets contain Co²⁺, Co³⁺, Ni²⁺, Ni³⁺, and Zn²⁺.

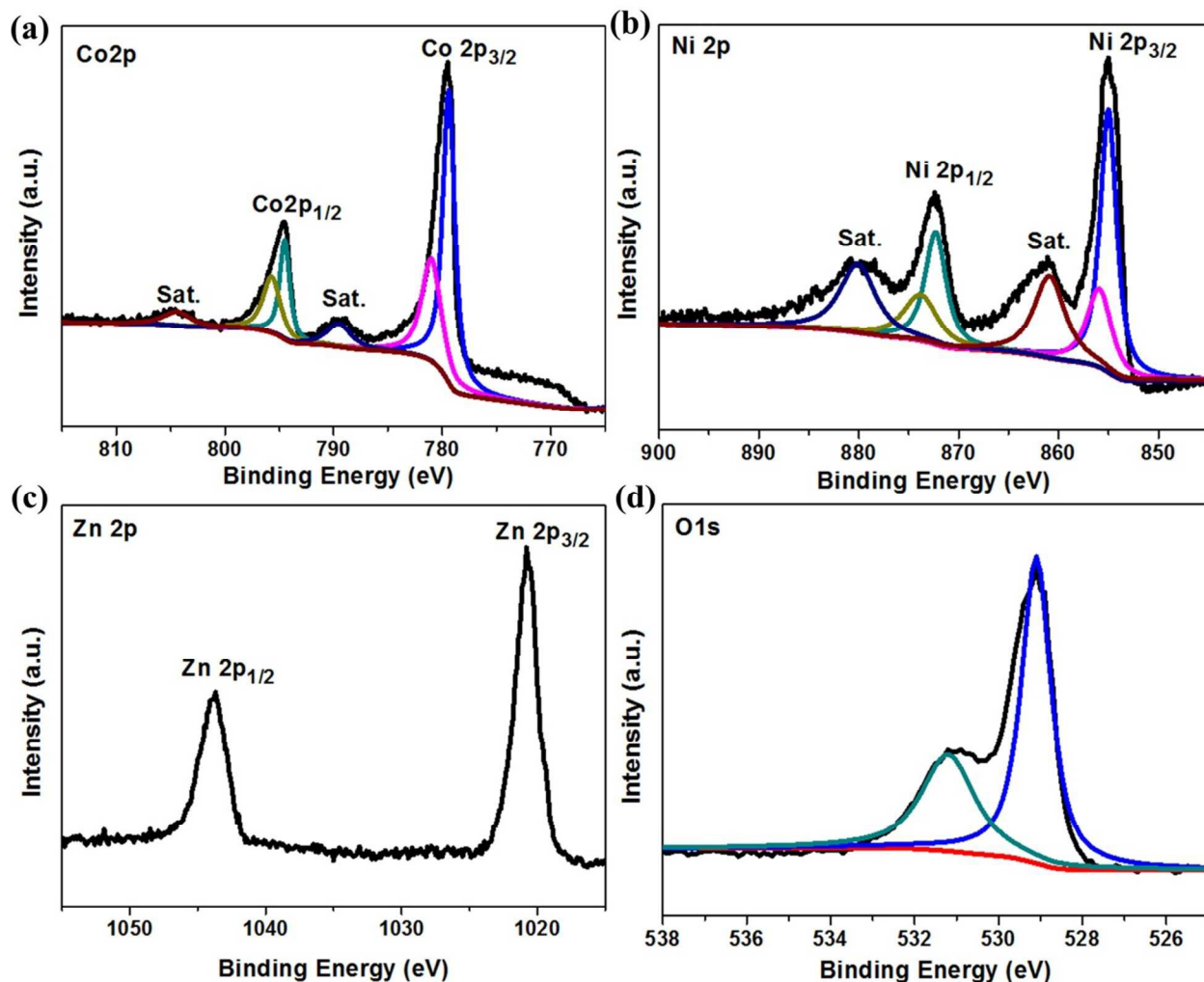


Figure 3. XPS spectra of (a) Co2p, (b) Ni2p, (c) Zn 2p and (d) O1s for ZNCO nanosheets.

The detailed microstructures and morphologies of the as-obtained ZNCO nanosheets were further examined through TEM, and the results are shown in Figure 4. The highly porous feature of the nanosheets is clearly distinguished from the TEM image (Figure 4(a)). These nanosheets feature a transparent, folded, and silk-like morphology, indicating the ultrathin nature. The dark strips are generally the folded edges or wrinkles of the nanosheets.³⁴ A magnified TEM image (Figure 4(b)) taken from the rectangular area marked in Figure 4(a) clearly demonstrates that these ultrathin nanosheets are highly porous but structurally continuous, constructed from

numerous nanoparticle subunits. This finding reveals that the thickness of the thin ZnCO nanosheet is approximately 4.2 nm. This type of ultrathin and mesoporous structure in the nanosheets is beneficial for electrolyte penetration and fast ion/electron transfer, which enhance electrochemical reactivity.³⁴ The HRTEM shown in Figure 4(c) reveals highly resolved lattice fringes with a measured interplanar spacing of 0.46 nm, which corresponds to the (111) plane of the spinel ZnCO phase.^{40,44,45} Many irregular well-defined pores dispersed in the interconnected framework of nanosheets are also clearly shown in Figure 4(c). The selected-area electron diffraction pattern in Figure 4(d) shows well-defined diffraction rings, which indicate the polycrystalline nature of these nanosheets and can be readily indexed to the (311), (400), and (440) crystal planes of the spinel ZnCO phase.³⁴

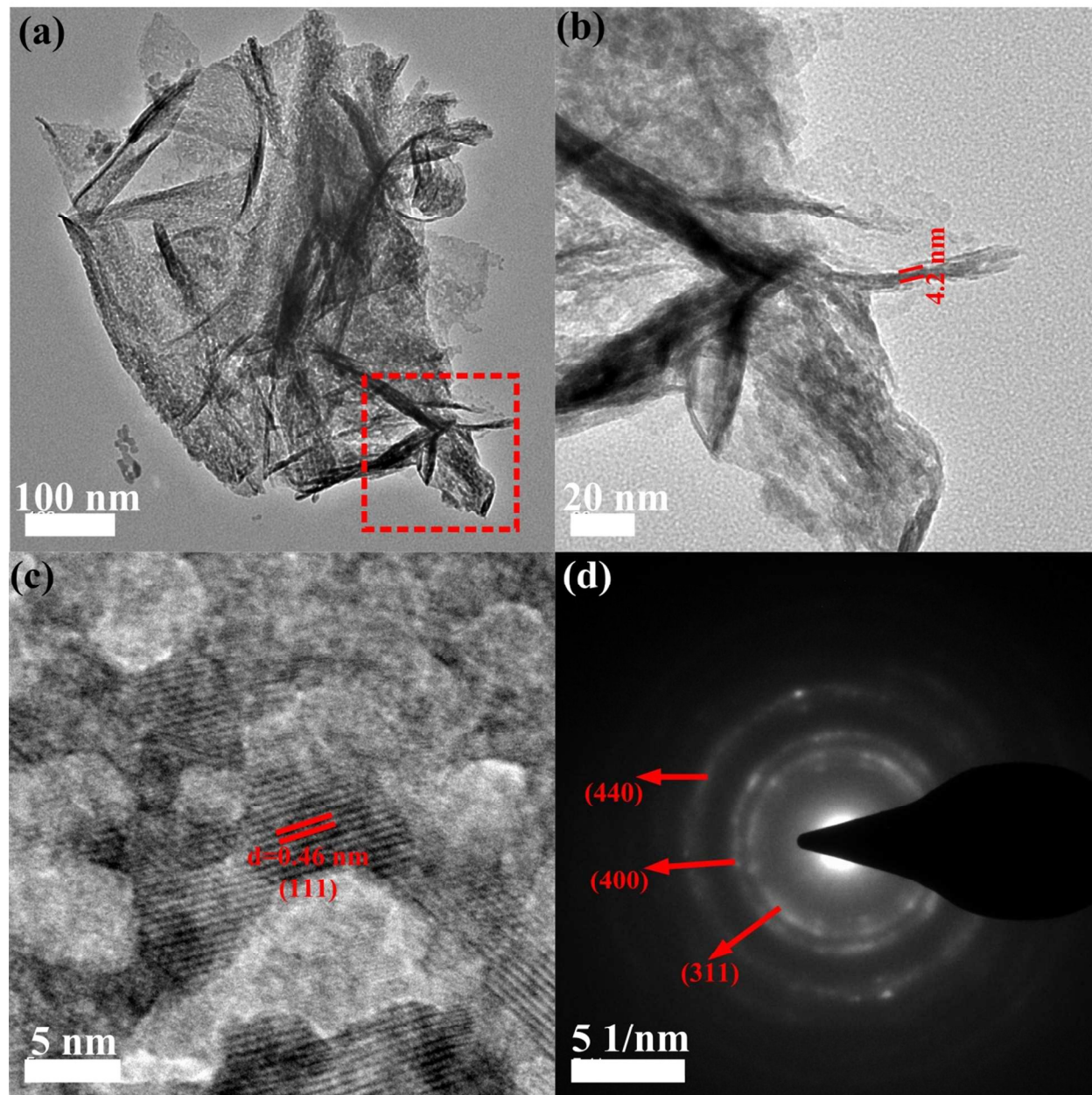


Figure 4. (a) Low-magnification TEM image of individual ZNCO nanosheets, (b) the enlarged TEM image taken from the rectangular area marked in (a), (c) HRTEM image of ZNCO nanosheets, and (d) the corresponding SAED pattern of ZNCO nanosheets.

The elemental distribution of the ZNCO nanosheets was investigated through elemental mapping analysis on a representative nanosheet under TEM observation. The corresponding element

mapping results (Figure 5) clearly elucidate the homogeneous distribution of Zn, Co, Ni, and O in the entire nanosheet, suggesting the successful formation of ternary ZNCO nanosheets.

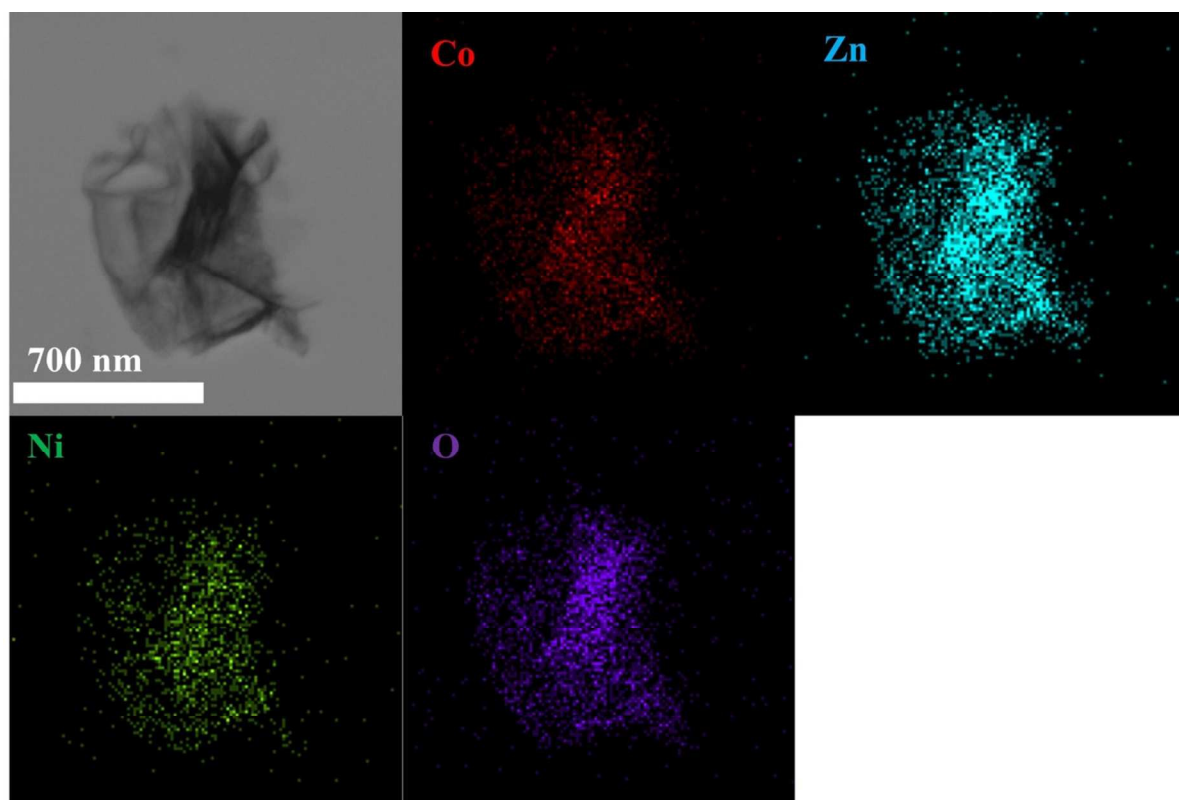


Figure 5. TEM-EDX mapping images of individual ZNCO nanosheets.

3.2. LIB performance evaluation

Enlightened by the advantageous structural features and compositional advantages of hierarchically porous ZNCO nanosheets, their Li storage properties were evaluated using coin-type cell configuration with Li metal as the counter electrode in the voltage window of 0.01–3.0 V. The results were compared with those of ZNCO nanosheet electrodes created using the traditional slurry-coating technique (Figure S3(c–d), supporting information). The first three cycles of the CV curves of the ZNCO nanosheets/Ni foam electrode are shown in Figure 6(a), which depicts an intense reduction peak at approximately 0.75 V in the first discharge process,

corresponding to the reduction of ZNCO to metallic Zn, Ni, and Co dispersed in an amorphous Li₂O matrix. Two weak reduction peaks at approximately 0.54 and 0.95 can be assigned to the formation of a LiZn alloy and solid electrolyte interphase (SEI).^{44,46–48} On the subsequent cathodic scans, two broad oxidation peaks appear at 1.68 and 2.29 V, which correspond to the oxidation of Zn, Ni, and Co nanograins to ZnO, NiO, and Co₃O₄, respectively.^{44,48} In the second cycle, the main reduction peak with significantly decreased intensity shifts to approximately 1.0 V and becomes broader compared with the first cycle, whereas the anodic process almost does not encounter any changes. From the second cycle onward, the reduction and oxidation peaks in the CV curves overlap very well, suggesting the high reversibility of Li storage. On the basis of the above analysis and CV results in accordance with the previously reported storage mechanism of NCO⁴⁶ and ZCO,⁴⁸ the electrochemical reactions of ZNCO referring to the discharge and charge processes can be clarified as follows (1–6):

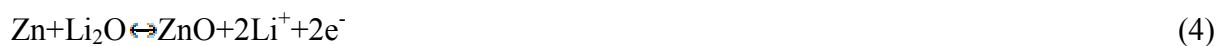
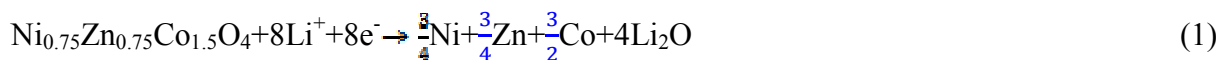


Figure 6(b) shows the discharge–charge curves of the electrode in the 1st, 2nd, 3rd, 10th, 20th, and 50th cycles performed in the voltage range of 0.01–3.0 V at a current density of 0.2 Ag⁻¹. As shown in Figure 5(b), the first discharge curve exhibits a long voltage plateau at 1.0–0.9 V,

followed by a gradual voltage decrease to the cutoff potential of 0.01 V, corresponding to the reduction of ZNCO to Zn, Ni, and Co, followed by Zn alloying with Li to LiZn. The discharging plateau becomes steeper and moves upward and is slightly higher than that of the first discharge curve in the subsequent cycles, which is consistent with the CV results and previous reports. The initial discharge and charge capacities are 1481 and 1105 mAh g⁻¹, respectively, which account for a coulombic efficiency of 74.6%, whereas the initial charge capacity and coulombic efficiency recorded at 0.1 Ag⁻¹ for the ZNCO nanosheet-pasted electrode (Figure S2(c)) are only marginally lower at 999 mAh g⁻¹ and 70%, respectively. The initial large capacity loss can be mainly ascribed to the possible irreversible processes, including electrolyte decomposition, inevitable formation of an SEI layer, and TMO reduction to metal with Li₂O formation, as reported by many authors.^{40,44,46,48} Nevertheless, the discharge–charge curve from the second cycle onward tends to be stable. The coulombic efficiency is also increased to above 96% from the fifth cycle and maintained above this value in the followed cycling processes, suggesting the good reversibility of the electrode.

The cycling performances of ZNCO/Ni foam over 50 cycles is presented in the voltage window of 0.01–3 V at a current density of 0.2 Ag⁻¹ in Figure 6(c). Interestingly, the ZNCO nanosheets/Ni foam electrode exhibits much higher reversible capacity and better cycling performance than the ZNCO nanosheet-pasted electrode (Figure S3(d), supporting information). The specific capacity of the ZNCO nanosheets/Ni foam electrode gradually increases from 1105 mAh g⁻¹ in the first cycle to 1296 mAh g⁻¹ in the 18th cycle and then slowly decreases to 1131 mAh g⁻¹ after 50 cycles, which is higher than the reported results of other TMO binder-free anodes (Table S2, supporting information). Meanwhile, the specific capacity of the ZNCO nanosheet-pasted electrode drops very rapidly from 999 in the first cycle to 161 after 50 cycles.

Consequently, the measured capacities of the ZNCO nanosheet-pasted electrode are noticeably lower than those of the ZNCO nanosheets/Ni foam electrode. The exceptionally improved cycling stability of the ZNCO nanosheets/Ni foam electrode may be attributed to the direct attachment and close contact of the hierarchically porous ZNCO nanosheet arrays on the 3D Ni foam that enables the full exposure of the active materials to the electrolyte, enhances ion and electron diffusion, and ensures good mechanical adhesion and electrical connection to the current collector.³⁷ The slight increase in capacity may be attributed to the gradual activation of active sites accessible to the Li⁺ storage^{42,49} and the measured specific capacities higher than the theoretical capacity of bulk ZNCO, which has also been widely observed in other TMOs.^{40,46,50} This phenomenon is likely because of the insertion of Li ions into interfacial storage that originated from the unique mesoporous feature of ZNCO associated with the reversible formation/dissolution of polymeric gel-like films after electrolyte degradation.^{40,50,51} More interestingly, the ZNCO nanosheet electrode demonstrates a higher reversible discharge capacity of ~1131 mAh g⁻¹ compared with the ZCO nanosheet electrode (Figure S4(f), supporting information), with a reversible capacity of ~909 mAh g⁻¹, whereas the NCO nanosheet electrode (Figure S4(c), supporting information) exhibits a reversible capacity of 881 mAh g⁻¹ after 50 cycles. This enhancement can be explained by the reason that the complementarities and synergies between different metallic elements of the ZNCO electrode in the Li discharge–charge process may enhance electrochemical performance.⁴⁴

The rate capability of the ZNCO nanosheets/Ni foam electrode was also measured, and the results are shown in Figure 6(d). The electrode exhibits the capacities of 1315, 1262, 987, and 759 after 10 cycles at rates of 0.1, 0.2, 0.5, and 1 Ag⁻¹, respectively. Even at a current density as high as 2 Ag⁻¹, the electrode can still deliver a reversible charge capacity of 546 mAh g⁻¹, which

is higher than the theoretical capacity of graphite (374 mAh g^{-1}). More importantly, the capacity of 1246 mAh g^{-1} can be retrieved when the current rate reverts to 0.2 Ag^{-1} , indicating its good structure stability. Aside from the high specific capacity and outstanding rate capability, the long-term cycling stability of the ZNCO nanosheets/Ni foam electrode at a high current density is also highly significant for practical applications of LIBs when fast discharge/charge is required. Thus, we further evaluated the ZNCO nanosheets/Ni foam electrode at a high current density of 1 Ag^{-1} (equal to 1C rate) over 1000 cycles. As shown in Figure 6(e), the capacity of the ZNCO nanosheets/Ni foam electrode gradually reduces to approximately 583 mAh g^{-1} after approximately 200 cycles. The capacity starts to increase gradually to a high value of 729 mAh g^{-1} during the subsequent 400 cycles and retains a value as high as 663 mAh g^{-1} after 1000 cycles, which is still much higher than the theoretical capacity of graphite (372 mAh g^{-1}). The observed rapid capacity fading at the initial 200 cycles may probably result from the lithiation-induced mechanical degradation accompanied by the decomposition and reformation of the electrolyte under a high discharge/charge current density.^{46,52} The slight increase in capacity, which is frequently observed in other TMO anodes,^{40,42,46,48,52} may be attributed to the gradual activation of active sites of porous ZNCO nanosheets accessible to the Li^+ storage and the reversible growth of the electrochemistry active polymeric gel-like film by the kinetically activated electrolyte degradation.^{42,52}

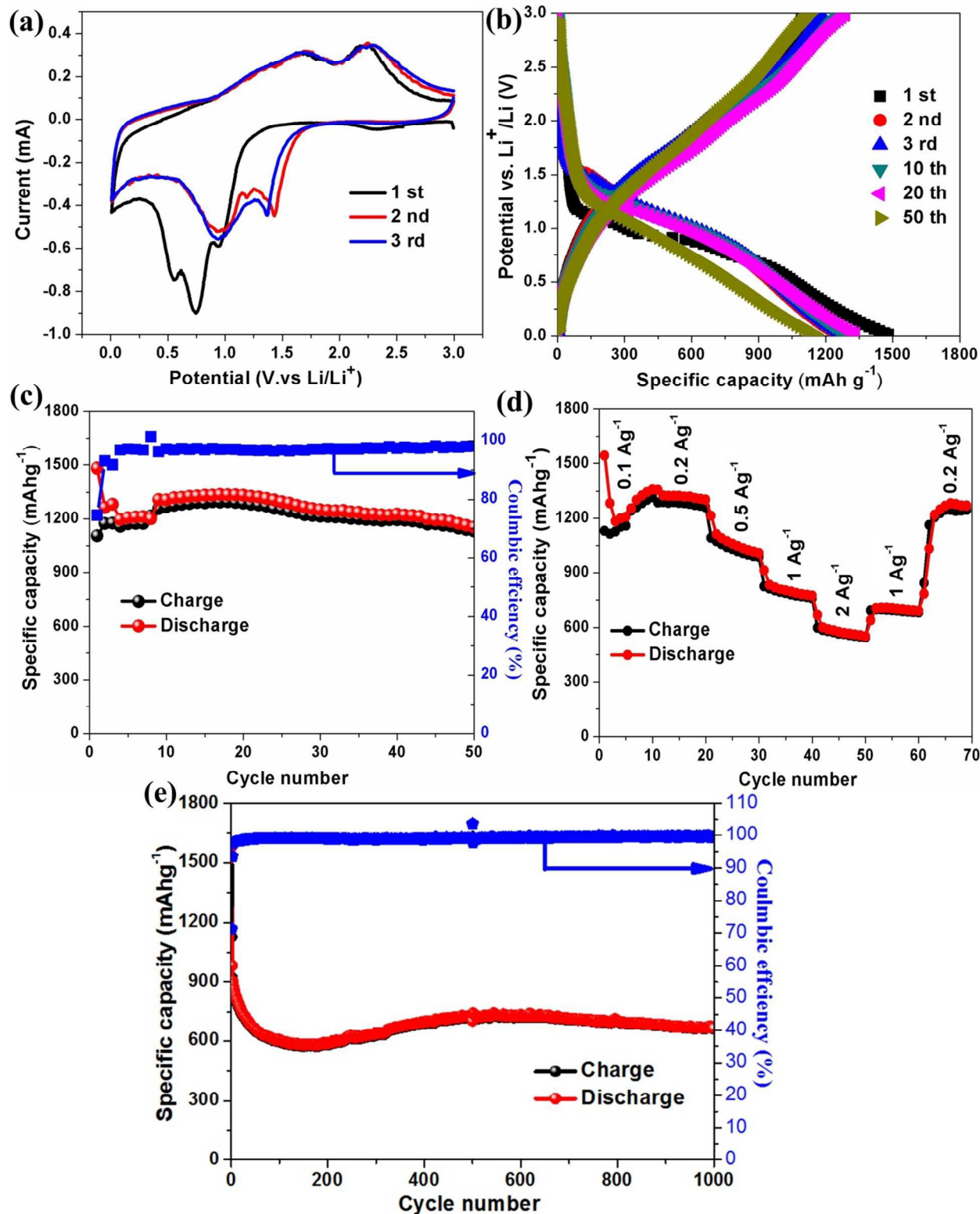


Figure 6. (a) CV curves of ZnCO nanosheets/Ni foam electrode in the potential range of 0.01–3 V at a scan rate of 0.1 mVs⁻¹ for the first three cycles, (b) typical discharge-charge voltage

profiles, (c) cycle performance of ZNCO nanosheets/Ni foam electrode at a current density of 0.2 Ag^{-1} , (d) rate capability of ZNCO nanosheets/Ni foam electrode at various current densities and (e) long-term cycling performance at current density of 1 Ag^{-1} for 1000 cycles after one cycle at a low current density of 0.1 Ag^{-1} .

3.3. SCs performance evaluation

CV and galvanostatic charge–discharge (GCD) tests were performed to investigate the electrochemical performances of the hierarchically porous structures of ZNCO nanosheet arrays directly grown on the Ni foam substrate as electrodes for SCs. The electrochemical performance of Co_3O_4 (CO), NCO and ZCO nanosheets grown on Ni foam as electrodes for SCs was also measured for comparison (Figure S5, supporting information). Figure 7(a) depicts the CV curves of the ZNCO nanosheets/Ni foam, ZCO nanosheets/Ni foam, NCO nanosheets/Ni foam and CO nanosheets/Ni foam electrodes in the potential range of 0–0.55 V versus Hg/HgO at a scan rate of 10 mV s^{-1} . Among the four electrodes, the ZNCO nanosheet electrode exhibits the largest increment in the CV-integrated area. This result indicates the largely enhanced electrochemical reaction activity of the ZNCO nanosheets electrode. Figure 7(b) shows the GCD curves of the ZNCO nanosheets/Ni foam, ZCO nanosheets/Ni foam, NCO nanosheets/Ni foam and CO nanosheets/Ni foam electrodes at a current density of 2 Ag^{-1} . It indicates that the ZNCO nanosheets/Ni foam electrode delivers the longest discharge time and thus exhibits the highest specific capacitance among the four electrodes. Figure 7(c) demonstrates the representative CV curves of the ZNCO nanosheets/Ni foam electrode within the potential range of 0–0.55 V versus Hg/HgO at scan rates ranging from 1 mV s^{-1} to 30 mV s^{-1} . As shown in Figure 7(c), one pair of redox peaks can be clearly observed, which is mainly attributed to the Faradaic redox reactions

related to M–O/M–O–OH (M represents Ni or Co) associated with OH[−] anions, indicating the capacitive features of the ZNCO nanosheet electrode.^{53–56} The shape of the CV curves basically remains unchanged except for the small shift in the peak position, and the peak current increases accordingly as the scan rate increases from 1 mV s^{−1} to 30 mV s^{−1} (30-fold increment in the sweep rate). These findings indicate the excellent electrochemical reversibility and outstanding high-rate performance of the electrode. GCD tests were then conducted at various current densities in the voltage region of 0–0.5 V (versus Hg/HgO), as shown in Figure 7(d). The nonlinear characteristics also further verify the capacitive behavior. The calculated specific capacitance of the ZNCO nanosheets/Ni foam electrode as a function of the discharge current density is plotted in Figure 7(e). The specific capacitance is as high as 1728, 1721, 1686, 1626, 1512, and 1240 Fg^{−1} at current densities of 1, 2, 5, 10, 20, and 50 Ag^{−1}, respectively, which are higher than those of the ZCO nanosheets/Ni foam (Figure S5(c), supporting information), NCO nanosheets/Ni foam (Figure S5(i), supporting information) and CO nanosheets/Ni foam electrodes (Figure S5(f), supporting information) under similar current densities, as well as the reported results in Table S3. Moreover, 72% of the capacitance is maintained when the discharge current density increases from 1 Ag^{−1} to 50 Ag^{−1}, indicating good rate capability. By contrast, only 60% of the capacitance of the ZCO nanosheets/Ni foam electrode (Figure S5(c), supporting information) is retained when the discharge current density increases from 1 Ag^{−1} to 20 Ag^{−1}. Considering that cycle stability is also an important factor in evaluating electrode performance, we also assessed the long-term cycling life of the hierarchically porous structures of the ZNCO nanosheets/Ni foam electrode through continuous GCD measurements at a current density of 20 Ag^{−1}; the results are shown in Figure 7(f). The figure illustrates an increased trend in electrode capacitance from the first cycle, which may be attributed to the gradual activation of the

electrode.^{57,58} Interestingly, the electrode of ZNCO nanosheets maintains a capacitance high up to 1655 Fg^{-1} with 108.6% retention after 5000 cycles, while the electrodes of ZCO nanosheets and NCO nanosheets just retain capacitance of 764 Fg^{-1} with 94.1% retention (Figure S6(a), supporting information) and 1106 Fg^{-1} with 91% retention (Figure S6(b), supporting information), respectively, indicating the outstanding cycling stability of the ZNCO electrode. In addition, the long-term electrochemical stability of ZNCO electrode is apparent from its very stable charge/discharge curve for the first and the last 10 cycles (inset of Figure 7(f)). The improved electrochemical performance of ZNCO electrode could be related to the compositional advantages and synergetic effects between different metallic elements of the ZNCO electrode,^{16,44} which may be understood from the following aspects. (1) The incorporation of foreign Zn^{2+} into the Co_3O_4 lattice could lead to a change in the chemical environment of Co ions. Zn^{2+} ions occupying tetrahedral sites increase the distance of the Co–O bonds. The change in the distance of Co^{3+} –O by Zn doping can enable the anions (OH^-) to adsorb onto the Co cations and thus facilitate the formation of Co^{4+} specie as follows: $\text{CoOOH} + \text{OH}^- \rightarrow \text{CoO}_2 + \text{H}_2\text{O} + \text{e}^-$.^{59–61} The creation of Co^{4+} species as active centers may contribute to the enhanced electrochemical reaction activity. Moreover, Zn doping is believed to be capable of contributing to the high active surface area by increasing active sites (Co^{3+}) on the surfaces of nanosheets.⁶⁰ Thus, the incorporation of Zn^{2+} ions has an effect on creating new active sites and promoting reaction species in accessing the oxidized cobalt ions to increase the number of oxidation state.^{60,62} (2) The incorporation of Ni element into the structure could produce more polarons and thus result in significant increase in electrical conductivity.^{59,63,64} Moreover, it offers rich redox reactions and enables multiple oxidation states resulted from the $\text{Ni}^{3+}/\text{Ni}^{4+}$ oxidation as well as from Ni^{2+} to Ni^{3+} , resulting in high electrochemical activity (more active redox states).^{63,64} (3)

The synergistic effects of the ternary metal components (Zn, Ni and Co) in the electrodes, such as Zn^{2+} -doping-induced $\text{Co}^{3+}/\text{Co}^{4+}$ oxidation, rich redox reactions offered from both the nickel and cobalt ions and the formation of mixed valence states at these multi-metal centers, all together contribute to the enhancement of the ZNCO electrode.^{16,59} Moreover, the resultant single-phase ZNCO with uniform distributions of Zn, Ni, Co, and O elements is not the mixtures of three single metal oxides (ZnO , NiO and Co_3O_4), but rather a new material with new functionalities and properties.

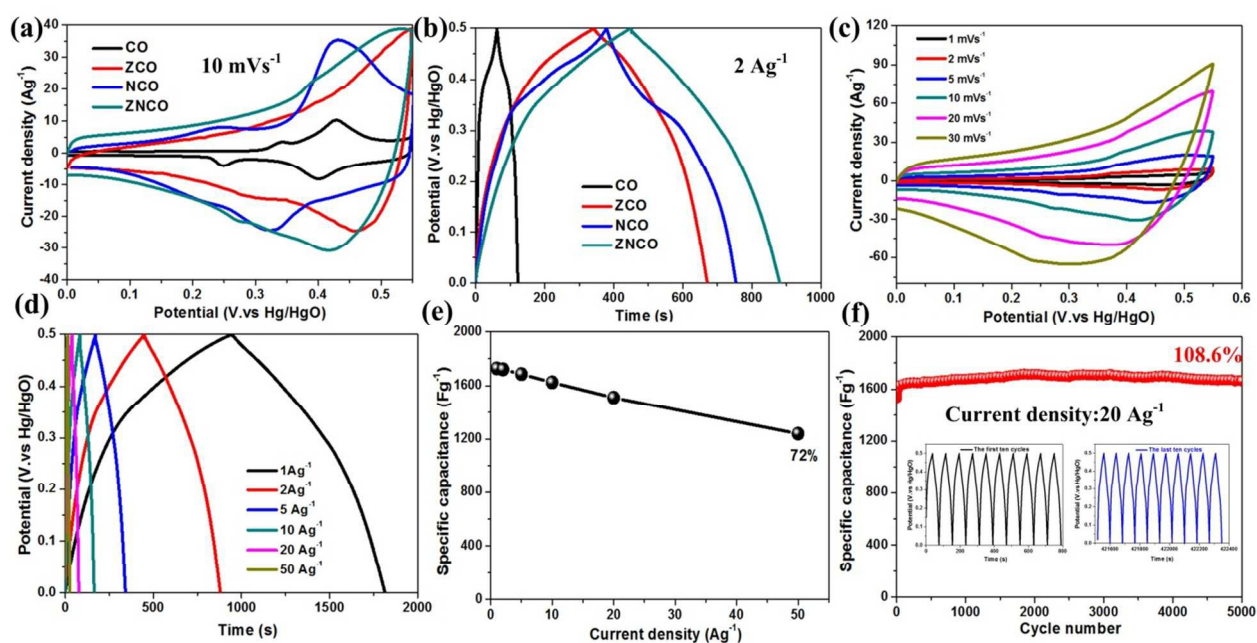


Figure 7. (a) CV curves of the ZNCO nanosheets/Ni foam, ZCO nanosheets/Ni foam, NCO nanosheets/Ni foam and CO nanosheets/Ni foam electrodes at scan rate of 10 mV s⁻¹, (b) charge-discharge curves of the ZNCO nanosheets/Ni foam, ZCO nanosheets/Ni foam, NCO nanosheets/Ni foam and CO nanosheets/Ni foam electrodes at current density of 2Ag⁻¹, (c) CV curves of the ZNCO nanosheets/Ni foam electrode at various scan rates ranging from 1 to 30 mV s⁻¹, (d) charge-discharge curves of ZNCO nanosheets/Ni foam electrode at various current densities, (e) the corresponding capacitance of ZNCO nanosheets/Ni foam electrode as a

function of current density, (f) cycling performance of the ZNCO nanosheets/Ni foam electrode at current density of 20 Ag^{-1} for 5000 cycles, inset is its corresponding charge/ discharge curves of the first ten and the last ten cycles for the 5000 cycles.

The enhanced electrochemical performances of ZNCO nanosheets on Ni foam as electrodes for both LIBs and SCs can be derived from the following advantageous structural features and compositional advantages. First, the porous feature of ZNCO nanosheets enables the full exposure of electroactive materials to the electrolyte, enhances ion and electron diffusion, and allows the robust storage of ions, thereby yielding a high capacity/capacitance.^{23,29,33} Second, the highly porous interconnected nanosheets consist of numerous highly crystalline nanoparticles that greatly facilitate electrolyte transport and increase the surface area, thereby promoting the electrolyte to easily diffuse into the inner region of the electrode.^{23,54} The array configuration of the hierarchically porous nanosheet possesses a favorable morphological and phase stability, which alleviates the structure or phase damage caused by volume expansion and redox reactions during the cycling process and may greatly contribute to excellent cycling stability.⁵⁴ Moreover, the direct attachment and close contact of ZNCO nanosheets on 3D Ni foam significantly enhance electrical conductivity because each nanosheet array tightly attaches to the current collector to form strong adhesion and electrical contact; this phenomenon creates an expressway for electric charge transfer and yields desirable rate capability.^{23,29} Finally, the complex chemical compositions and their synergetic effects among different metallic elements in ZNCO nanosheets strengthen electrochemical activities and thus enhance electrochemical performance.⁴⁴

4. Conclusion

ZNCO nanosheets with 3D hierarchically porous architectures were successfully grown on Ni foam through a facile and efficient CBD process followed by a thermal treatment. The as-synthesized nanostructures were directly used as a binder-free electrode for high-performance energy storage devices. The unique architecture consisting of ZNCO nanosheets with a thickness of a few nanometers provides open channels for efficient ion transport and a large surface area for electrochemical reactions, which greatly enhance the specific capacity/capacitance, cycling stability, and rate capability of the electrode. When used as an electrode in LIBs, these nanosheets deliver a reversible capacity of 1131 mAh g⁻¹ after 50 cycles at a current density of 0.2 Ag⁻¹ and exhibit an excellent long-term cycling stability (capacity of up to 622 mAh g⁻¹ at a high current density of 1 Ag⁻¹ even after 1000 cycles) and an outstanding rate capability. When used as an electrode in SCs, these nanosheets exhibit a high specific capacitance (1728 Fg⁻¹ at 1 Ag⁻¹), an outstanding rate capability, and a superior cycling stability (capacitance of 1655 Fg⁻¹ after 5000 cycles at 20 Ag⁻¹ with 108.6% retention). The synthesis strategy and design concept are also applicable to other TMOs for high-performance electrochemical energy storage.

Acknowledgments

This work was supported by National Basic Research Program of China (973 program, Grant No. 2011CB935903), National Natural Science Foundation of China (Grant No. 21233004 and 21021002) and Hong Kong Research Grants Council (Grant no. CityU 125412), NSAF (Grant No. U1330132).

References

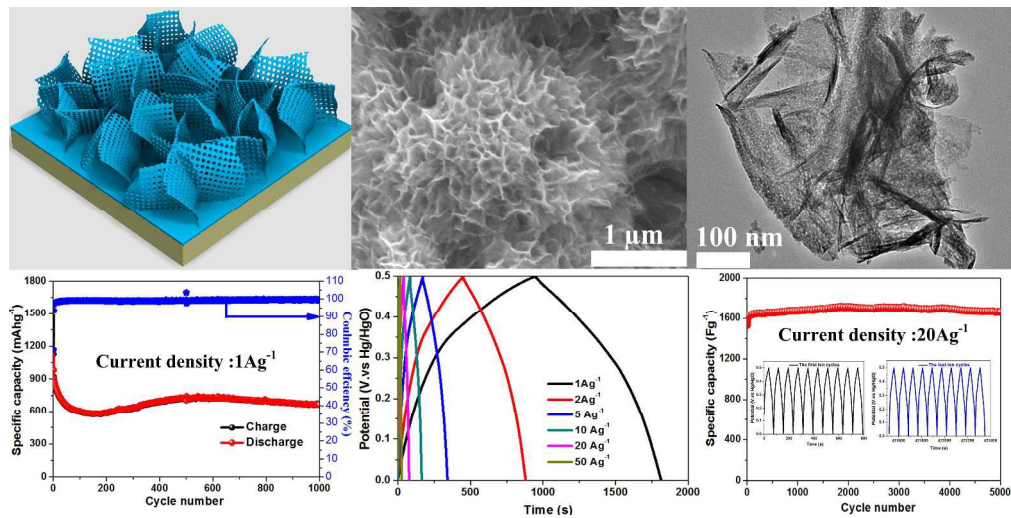
1. M.-K. Song, S. Park, F. M. Alamgir, J. Cho, and M. Liu, *Mater. Sci. Eng. R Reports*, 2011, **72**, 203–252.
2. S. Goriparti, E. Miele, F. De Angelis, E. Di Fabrizio, R. Proietti Zaccaria, and C. Capiglia, *J. Power Sources*, 2014.
3. D. Liu and G. Cao, *Energy Environ. Sci.*, 2010, **3**, 1218.
4. C. Wu and Y. Xie, *Energy Environ. Sci.*, 2010, **3**, 1191–1206.
5. G.-N. Zhu, Y.-G. Wang, and Y.-Y. Xia, *Energy Environ. Sci.*, 2012, **5**, 6652.
6. A. S. Aricò, P. Bruce, B. Scrosati, J.-M. Tarascon, and W. van Schalkwijk, *Nat. Mater.*, 2005, **4**, 366–77.
7. B. Dunn, H. Kamath, and J.-M. Tarascon, *Science*, 2011, **334**, 928–35.
8. X. Meng, X.-Q. Yang, and X. Sun, *Adv. Mater.*, 2012, **24**, 3589–3615.
9. L. Ji, Z. Lin, M. Alcoutlabi, and X. Zhang, *Energy Environ. Sci.*, 2011, **4**, 2682.
10. J. Jiang, Y. Li, J. Liu, X. Huang, C. Yuan, and X. W. Lou, *Adv. Mater.*, 2012, **24**, 5166–5180.
11. Y.-G. Guo, J.-S. Hu, and L.-J. Wan, *Adv. Mater.*, 2008, **20**, 2878–2887.
12. K. T. Lee and J. Cho, *Nano Today*, 2011, **6**, 28–41.
13. D. Deng, M. G. Kim, J. Y. Lee, and J. Cho, *Energy Environ. Sci.*, 2009, **2**, 818.
14. D. Wang, J. Yang, X. Li, D. Geng, R. Li, M. Cai, T.-K. Sham, and X. Sun, *Energy Environ. Sci.*, 2013, **6**, 2900.

15. M. Kundu, C. C. A. Ng, D. Y. Petrovykh, and L. Liu, *Chem. Commun. (Camb)*., 2013, **49**, 8459–61.
16. C. Yuan, H. Bin Wu, Y. Xie, and X. W. Lou, *Angew. Chemie - Int. Ed.*, 2014, **53**, 1488–1504.
17. B. L. Ellis, P. Knauth, and T. Djenizian, *Adv. Mater.*, 2014, **26**, 3368–3397.
18. M. Kundu and L. Liu, *J. Power Sources*, 2013, **243**, 676–681.
19. Y. Li, H. Zhang, and P. Kang Shen, *Nano Energy*, 2015, **13**, 563–572.
20. Y. Xu, G. Jian, Y. Liu, Y. Zhu, M. R. Zachariah, and C. Wang, *Nano Energy*, 2014, **3**, 26–35.
21. X. Xu, R. Cao, S. Jeong, and J. Cho, *Nano Lett.*, 2012, **12**, 4988–4991.
22. F. Li, Q.-Q. Zou, and Y.-Y. Xia, *J. Power Sources*, 2008, **177**, 546–552.
23. G. Zhang and X. Lou, *Adv. Mater.*, 2012, **25**, 976–979.
24. V. Augustyn, P. Simon, and B. Dunn, *Energy Environ. Sci.*, 2014, **7**, 1597.
25. Y. Zhang, L. Li, H. Su, and X. Dong, *J. Mater. Chem. A Mater. energy Sustain.*, 2014, **3**, 43–59.
26. X. Fan, J. Shao, X. Xiao, X. Wang, S. Li, H. Ge, L. Chen, and C. Wang, *J. Mater. Chem. A*, 2014, **2**, 18367–18374.
27. Y. Li, Q. Zhang, J. Zhu, X.-L. Wei, and P. K. Shen, *J. Mater. Chem. A*, 2014, **2**, 3163.
28. M. Kundu and L. Liu, *Mater. Lett.*, 2015, **144**, 114–118.
29. L. Shen, Q. Che, H. Li, and X. Zhang, *Adv. Funct. Mater.*, 2013, DOI: 10.1002/adfm.201303138.
30. Y. Ding, Y. Yang, and H. Shao, *Electrochim. Acta*, 2011, **56**, 9433–9438.

31. Y. Ding, Y. Yang, and H. Shao, *Solid State Ionics*, 2012, **217**, 27–33.
32. G. Zhang, H. Wu, H. Hoster, M. Chan-Park, and X. Lou, *Energy Environ. Sci.*, 2012, **5**, 9453.
33. X. Xia, J. Tu, Y. Zhang, X. Wang, C. Gu, X. Zhao, and H. Fan, *ACS Nano*, 2012, **6**, 5531–5538.
34. C. Yuan, J. Li, L. Hou, X. Zhang, L. Shen, and X. Lou, *Adv. Funct. Mater.*, 2012, **22**, 4592–4597.
35. S. Peng, L. Li, H. Bin Wu, S. Madhavi, and X. W. D. Lou, *Adv. Energy Mater.*, 2014, 1–7.
36. B. Liu, J. Zhang, X. Wang, G. Chen, D. Chen, C. Zhou, and G. Shen, *Nano Lett.*, 2012, **12**, 3005–3011.
37. B. Qu, L. Hu, Q. Li, Y. Wang, L. Chen, and T. Wang, *ACS Appl. Mater. Interfaces*, 2014, **6**, 731–6.
38. L. Yu, L. Zhang, H. Bin Wu, G. Zhang, and X. W. (David) Lou, *Energy Environ. Sci.*, 2013, **6**, 2664.
39. Q. Yang, Z. Lu, J. Liu, X. Lei, Z. Chang, L. Luo, and X. Sun, *Prog. Nat. Sci. Mater. Int.*, 2013, **23**, 351–366.
40. Y. Xiao, C. Hu, and M. Cao, *J. Power Sources*, 2014, **247**, 49–56.
41. W. Mei, J. Huang, L. Zhu, Z. Ye, Y. Mai, and J. Tu, *J. Mater. Chem.*, 2012, **22**, 9315.
42. Y. Jiang, Z.-J. Jiang, L. Yang, S. Cheng, and M. Liu, *J. Mater. Chem. A*, 2015, **3**, 11847–11856.

43. X. Xiong, G. Waller, D. Ding, D. Chen, B. Rainwater, B. Zhao, Z. Wang, and M. Liu, *Nano Energy*, 2015, **16**, 71–80.
44. X. Song, Q. Ru, Y. Mo, L. Guo, S. Hu, and B. An, *J. Power Sources*, 2014, **269**, 795–803.
45. S. Choi and Y. Kang, *ChemSusChem*, 2013, **6**, 2111–2116.
46. J. Li, S. Xiong, Y. Liu, Z. Ju, and Y. Qian, *ACS Appl. Mater. Interfaces*, 2013, **5**, 981–988.
47. N. Wang, X. Ma, H. Xu, L. Chen, J. Yue, F. Niu, J. Yang, and Y. Qian, *Nano Energy*, 2014, **6**, 193–199.
48. W. Luo, X. Hu, Y. Sun, and Y. Huang, *J. Mater. Chem.*, 2012, **22**, 8916.
49. X. Rui, H. Tan, D. Sim, W. Liu, and C. Xu, *J. Power Sources*, 2012, **222**, 97–102.
50. J. Bai, X. Li, G. Liu, Y. Qian, and S. Xiong, *Adv. Funct. Mater.*, 2014, DOI: 10.1002/adfm.201303442.
51. L. Hu, N. Yan, Q. Chen, and P. Zhang, *Chem. A Eur. J.*, 2012, **18**, 8971–8977.
52. H. Sun, G. Xin, T. Hu, M. Yu, D. Shao, X. Sun, and J. Lian, *Nat. Commun.*, 2014, **5**, 4526.
53. J. Zhou, Y. Huang, X. Cao, B. Ouyang, W. Sun, C. Tan, Y. Zhang, Q. Ma, S. Liang, Q. Yan, and H. Zhang, *Nanoscale*, 2015, 7035–7039.
54. Y. Chen, B. Qu, L. Hu, Z. Xu, Q. Li, and T. Wang, *Nanoscale*, 2013, **5**, 9812–20.
55. G. Zhang and X. Lou, *Sci. Rep.*, 2013, **3**, 1470.

56. J. Xu, L. Han, X. Liu, J. Kim, and Y. Luo, *Phys. Chem. Chem. Phys.*, 2015, **17**, 17016.
57. W. Zhou, D. Kong, X. Jia, C. Ding, C. Cheng, and G. Wen, *J. Mater. Chem. A*, 2014, **2**, 6310.
58. D. Cheng, Y. Yang, J. Xie, C. Fang, G. Zhang, and J. Xiong, *J. Mater. Chem. A*, 2015, **3**, 14348–14357.
59. X. Zhang, J. Zhang, and K. Wang, *ACS Appl. Mater. Interfaces*, 2015, **7**, 21745–21750.
60. X. Liu, Z. Chang, L. Luo, T. Xu, X. Lei, J. Liu, and X. Sun, *Chem. Mater.*, 2014, **26**, 1889–1895.
61. X. Zou, A. Goswami, and T. Asefa, *J. Am. Chem. Soc.*, 2013, **135**, 17242–17245.
62. P. Yuan, N. Zhang, D. Zhang, T. Liu, L. Chen, X. Liu, R. Ma, and G. Qiu, *Chem. Commun.*, 2014, **50**, 11188.
63. D. P. Dubal, P. Gomez-Romero, B. R. Sankapal, and R. Holze, *Nano Energy*, 2015, **11**, 377–399.
64. Z. Wu, Y. Zhu, and X. Ji, *J. Mater. Chem. A*, 2014, **2**, 14759–14772.



451x229mm (300 x 300 DPI)